Accepted Manuscript


AC Voltage Induced Electrohydrodynamic Two-Phase Convective Boiling Heat Transfer in Horizontal Annular Channels

J.S. Cotton, A.J. Robinson, M. Shoukri, J.S. Chang

PII: S0894-1777(12)00070-2
DOI: 10.1016/j.expthermflusci.2012.03.003
Reference: ETF 7677

To appear in: *Experimental Thermal and Fluid Science*

Received Date: 12 October 2010
Revised Date: 4 March 2012
Accepted Date: 5 March 2012

Please cite this article as: J.S. Cotton, A.J. Robinson, M. Shoukri, J.S. Chang, AC Voltage Induced Electrohydrodynamic Two-Phase Convective Boiling Heat Transfer in Horizontal Annular Channels, *Experimental Thermal and Fluid Science* (2012), doi: 10.1016/j.expthermflusci.2012.03.003

# AC Voltage Induced Electrohydrodynamic Two-Phase Convective Boiling Heat Transfer in Horizontal Annular Channels

**J.S. Cotton[1,*], A. J. Robinson[1,2], M. Shoukri [1], J.S. Chang[3]**

1) McMaster University, Department of Mechanical Engineering, Hamilton, Ontario, Canada.
2) Trinity College Dublin, Department of Mechanical and Manufacturing Engineering, Dublin, Ireland.
3) McMaster University, McIARS, and Department of Engineering Physics, Hamilton, Ontario, Canada.

* Corresponding Author:
McMaster University, Department of Mechanical Engineering, 1280 Main Street W., Hamilton, Ontario, Canada, L8S-4L7, T: 1-905-525-9140 Ext. 24899, F: 1-905-572-7944
cottonjs@mcmaster.ca

## Abstract

An experimental study of alternating current (AC) induced electrohydrodynamic (EHD) flow and heat transfer augmentation for boiling inside an annular channel containing working fluid refrigerant HFC-134a has been conducted in a single-pass, counter-flow heat exchanger with a rod electrode placed concentric to a grounded tube. Experiments were conducted for an inlet quality of 0%, a heat flux of 10.2 kW/m$^2$, mass fluxes from 100 kg/m$^2$s to 500 kg/m$^2$s and applied voltages from 0 kV to 8 kV DC and 0 kV to 24 kV peak to peak AC. The AC tests were conducted for both low frequency (60 Hz) and high frequency (6.6 kHz) near sinusoidal waveforms. The results show that there is no apparent difference between the DC and the 6.6 kHz AC test cases, whereas the 60 Hz AC tests show significantly different behaviour. The flow boiling heat transfer results indicate that the averaged heat transfer coefficients can be increased by as much as 3-fold for a 24 kV p.p. 60 Hz AC applied voltage. This also incurs a pressure drop penalty of 2.6 fold across the heat exchanger.

**Keywords** Electrohydrodynamic, AC Alternating Current, Heat Transfer, Convective Boiling, Flow Pattern, Two-Phase

## 1. Introduction

The subject of heat transfer enhancement has developed into an intense field of study over the past 30 years in response to the demands imposed by the military, automotive, space, power generation, HVAC and thermal industrial applications for more effective and compact heat exchangers. Virtually every heat exchanging device is a potential candidate for enhanced heat transfer. This being the case, a variety of methods have been proposed and implemented for the purpose of increasing heat transfer coefficients in heat exchangers. The majority of augmentation techniques focus on the disruption and destabilization of the thermal boundary layer in single-phase applications and augmented boiling/condensation and flow dynamics near the heat transfer surface where two-phase flow is concerned. Among the many techniques that show promise for heat transfer enhancement is *electrohydrodynamics* (EHD). In the context of two-phase flow heat transfer enhancement, the EHD technique utilizes a high voltage to create a dynamic electric field to alter the flow regime creating increased mixing of the flow and/or phases and improved wetting of the heat transfer surface.

Interest in this heat exchange augmentation technique arises largely due to the unique benefits that it exhibits. The potential advantages that EHD is envisioned to provide are: improved system performance, improved energy efficiency, reduced system weight, volume, material and costs.

Previous research on EHD augmentation of flow boiling and condensation has shown that the electric field influences on two-phase systems are due to the addition of electrical body forces to the flow. These electric forces imposed on the flow field can be represented by the expression [1, 2]:

$$\overline{f_E} = \rho_{ei}\overline{\mathbf{E}} - \frac{1}{2}E^2\nabla\varepsilon + \frac{1}{2}\nabla[\rho E^2(\frac{\partial\varepsilon}{\partial\rho})_T] \qquad (1)$$

The three terms on the right-hand side of Equation (1) represent the *electrophoretic*, *dielectrophoretic* and *electrostrictive* components of the force, respectively. The *electrophoretic* force is due to the net free charge existing within the fluid or which has been injected from the electrodes. The *dielectrophoretic* force is a consequence of inhomogeneity or spatial change in the permittivity of the dielectric fluid. This can be caused by non-uniform electric fields, temperature gradients, and differences in fluid properties such as those which exist between a vapour and liquid. The *electrostrictive* force is caused by inhomogeneous electric field strength and the variation in dielectric constant with temperature and density.

In single phase applications where there is not significant temperature difference in the working fluid, the electrostriction force which accounts for property gradients is negligible due to the small dielectric constant gradient [3,4,5,6,7]. In an attempt to identify the relative importance of the other two electrical forces, Cotton et al. [8] performed a dimensional analysis and concluded that for the DC applied voltages of their tests the *dielectrophoretic* component was dominant over the *electrophoretic*. In a two-phase flow the *dielectrophoretic* component of the force can be substantial at vapour-liquid interfacial regions due to a step change in the permittivity. This results in a force which draws the liquid phase to regions of high electric field strength, referred to as the *liquid extraction phenomenon*. This may be quite beneficial with regard to heat transfer enhancement of stratified or condensing flows as the layer thickness can be decreased [9,10,11]. Even still, care must be taken since, depending on the mass flux, some studies have shown that the liquid extraction phenomena may promote early partial dryout which can have an unfavourable effect on the heat transfer [12, 13]. Regardless, the application of an electric field can cause flow regime transitions that positively or negatively influence the heat transfer. This last point is crucial since EHD may afford the opportunity to develop novel active control technologies for heat exchangers.

There have been several studies on EHD heat transfer enhancement and reviews are given by Jones [3], Allen and Karayiannis [15], Seyed-Yagoobi and Bryan [16] and Laohalertdecha et al. [17]. The preponderance of the previous studies considered the influence of DC electric fields on to two-phase convective boiling and condensation. Experiments involving EHD augmented heat transfer in horizontal tube-side flow boiling have been conducted by Yabe et al. [18], Singh et al. [12,19], Salehi et al. [20], Norris et al. [13], Seyed-Yagoobi and Bryan [15], Bryan and Seyed-Yagoobi [21], and Cotton et al. [8, 9]. Even though previous investigations are in qualitative agreement, the level of time averaged heat transfer coefficient enhancement depends on test-specific factors such as the experimental facility and working fluids used, the range of mass fluxes tested, the electrode configurations etc. It can generally be said that enhancement levels range between 1.6 fold [9] to as high as 5.5 fold [12,19]. However, no comprehensive investigation on the influence of AC electric fields on the thermal-hydraulics of EHD augmented convective boiling has been reported. Work has been conducted on the effect of AC applied voltages on pool boiling by some investigators [2,3,22,23] and bubble synchronization with varying AC frequencies was observed with heat transfer enhancement. A similar synchronization of frequency and heat transfer coefficient has been observed in single phase natural convection [24]. Carrying on from the DC work with condensing two-phase flow [25], Sadek et al. [11] and Cotton [26] have shown that the flow regime and the interaction between the stratum of liquid and the electrode can be very dependent on the magnitude and frequency of the applied voltage. Recently, AC high voltage sine and square waves were applied for tube-side condensation of flowing refrigerant HFC-134a and the effects on the heat transfer and pressure drop were investigated [27].

This experimental investigation considers AC voltages applied to convective boiling in a horizontal tube with a concentric electrode. Both quasi-local and overall average heat transfer coefficients are measured along with the pressure drop across the channel. Comparisons of the heat transfer and pressure drop are made between the field-free baseline tests and both DC and AC applied voltage tests for a range of test conditions.

## 2. Experimental Facility and Data Reduction

### 2.1 The Experimental Two-Phase Flow Facility

Fig. 1 illustrates a schematic of the instrumented test facility used in this investigation. The facility utilizes refrigerant HFC-134a (R134a) as the working fluid which is circulated by a gear pump in a closed loop. The test facility consists of three main sections: the preheater, the test section and the condenser. The preheat stage uses an electrical heater to increase the refrigerant temperature to slightly below that of the saturation temperature corresponding with the system pressure to ensure that local dryout does not occur. The flow is then routed to a flat plate fluid-fluid heat exchanger which raises the refrigerant to the saturation temperature and, if required, boils the working fluid generating a quality in excess of unity at the entrance of the test section. Knowing the thermodynamic state of the refrigerant at the exit of the pump together with the total heat input from the two preheat stages allows for the determination of its thermodynamic state at the entrance of the test section. In this way, the inlet refrigerant quality can be monitored and controlled. The refrigerant is then routed to the test section preceded by a

1.0 m (90-diameters) long adiabatic developing section to ensure fully developed flow at the entrance of the test section.

The test section is a horizontally mounted counter-flow tube-and-shell heat exchanger. The two-phase refrigerant flows within the tube-side and is heated by hot water flowing in the annular shell of the heat exchanger. The two-phase refrigerant then exits the test section and is returned to its original subcooled state using a water-cooled condensing heat exchanger. Subcooling the refrigerant ensures that vapour does not enter the gear pump.

Of principal importance for this investigation are the measurements of water and refrigerant mass flow rates, the pressure drop across the test section as well as temperature measurements as indicated in Fig. 1. The calibrated uncertainty of the thermocouples was ±0.1$^{o}$C. To guarantee adequate accuracy of the refrigerant mass flux up to 500 kg/m$^2$s, a low range (0 - 0.02 kg/s ± 0.00004 kg/s) and a high range (0.028 - 0.28 kg/s ± 0.0001 kg/s) turbine flow meter was used. The differential pressure transducer was calibrated to an accuracy of ± 8Pa.

### 2.2 The Test Section

A more detailed view of the test section is given in Fig. 2. The test section consisted of concentric tubes arranged so as to create a 1.5 m long single-pass counter-flow heat exchanger. The inner tube contained the two-phase R134a mixture and was fabricated from a 1.8 m long stainless steel tube of 12.7 mm outside diameter and 10.92 mm inside diameter. The outer jacket contained a measured flow of heated water as the heat source for evaporating the refrigerant. The outer tube was 1.5 m in length, with an inner diameter of 20.8 mm and an outside diameter of 26.7 mm. The water-side of the heat exchanger was treated as 6 discrete sections, each 250 mm in length. Each section had thermocouples at the entrance and exit of the water and centrally located wall mounted thermocouples on the refrigerant-side tube wall. Each individual section was then divided into top and bottom sections, in the sense that inlet and outlet water and wall temperatures were monitored for each the top and bottom sections. This resulted in a total of 12 discrete sections, 6 top and 6 bottom, where the heat transfer and wall temperatures are measured and were used to estimate quasi-local time averaged heat transfer coefficients as well as give an indication of transient flow regime behavior through assessment of the wall superheat. The local wall temperature measurements were facilitated by 0.5 mm diameter sheathed type T thermocouple probes which were inserted into 25 mm × 0.5 mm grooves, cut to a depth of 0.5 mm along the length of the test section. The thermocouples were silver-soldered in place. The axial water temperature distribution was measured at five top and bottom locations in addition to both inlet and outlet, as depicted in Fig. 2.

The coaxial electrode was fabricated from a 3.175 mm diameter stainless steel rod. Concentric alignment of the electrode was maintained by using five non-conducting spacers strategically placed to minimize interference with the surface temperature thermocouples. The pressure drop across the test section was measured by a Validyne differential pressure transducer with a 34.47 kPa (5 psi) diaphragm. High speed video imagining of the flow regime at the exit of the test section was performed at 1000 frames/s by a high speed camera.

### 2.3 Electrical Characteristics of R-134a

Table 1 presents the relevant electrical properties of R-134a reported in the published literature.

The discrepancies between the various studies are believed to be due to the level of impurities in the sample tested. As discussed by Meurer et al. [30] and Richard [34], the resistivity may be dependent on the absorbed water content and other impurities in HFC's and such deviations are a possible consequence. In the current study, the dielectric constant of $\varepsilon_l$ = 9.42 was adopted based on the data available and capacitance measurements conducted in the test section. The volume electrical resistance presented by Sekiya and Misaki [32] was used based on the test conditions (22ºC at 1.57MPa) and as their data was the reference benchmark by Spatz and Minor [35].

### 2.4 AC Waveforms

The voltage potential for the DC experiments was supplied by a Glassman high voltage power supply; Series EL model EL30R1.5, with reversible polarity up to 30 kV. The voltage was set to the target voltage by means of a potentiometer. The accuracy was 1% of rated load + 1% of setting with a ripple better than 0.03% RMS of rated voltage at full load. For the low and high frequency AC experiments performed, the electric field was generated by a 60 Hz (0 - 25 kV peak to peak) Kyoto Denkiki (HV - 10A) power supply and a Jefferson Magnetek 6.6 kHz (9 kV peak to peak) transformer in series with a 120 V variable transformer.

Current measurements were performed by either an Armaco® 0 - 25 µA analog current meter or an IPC® wide band current transformer 1mA (CM-01-L) for the DC and AC experiments, respectively. The voltage and current waveforms were recorded with a Tektronix 200 MHz digital oscilloscope (TDS 420A) via a high voltage probe. Fig. 3 presents typical low and high frequency AC waveforms. It is evident that the applied voltage waveforms are distorted sinusoidal waveforms and result in some displacement current based on the present electrode arrangement and phase distributions. No conduction current was observed based on the analog current meter used.

## 3. Data Reduction and Uncertainty

### 3.1 Time Averaged Heat Transfer Coefficient

As mentioned, the test section was discretized into 12 sections; 6 along the top and 6 along the bottom. To provide more detail with regard to the influence of EHD on the flow regime and subsequent heat transfer, each section was treated individually. For each section it was assumed that the wall heat flux was uniform along its surface and could be determined by the total heat transfer to the refrigerant along that section, determined by:

$$q''_{i \to i+1} = \frac{q_{i \to i+1}}{A_i} = \frac{\dot{m}_w c_{pw}}{\pi D_o L_i} (T_{W_{i+1}} - T_{W_i}) \qquad (2)$$

where $L_i$ is the length of the individual section, $D_o$ is the outer diameter of the inner stainless steel tube and the temperature difference is determined by taking the mean of the time averaged top and bottom water temperatures at the outlet and inlet of each section and subtracting them. With the local heat flux approximated for each section, the local refrigerant-side heat transfer coefficients for each the top and bottom portions of the section were approximated by the following:

$$h_{i_t} = \frac{q''_{i \to i+1}}{(T_{i-S_t} - T_{sat})} \quad , \quad h_{i_b} = \frac{q''_{i \to i+1}}{(T_{i-S_b} - T_{sat})} \qquad (3)$$

where the temperature differences on the denominators represent the difference between the measured local top ($T_{i\text{-}St}$) and bottom ($T_{i\text{-}Sb}$) wall temperature and the saturation temperature ($T_{sat}$) of the refrigerant. The overall heat transfer coefficient is then determined by averaging all of the 12 top and bottom heat transfer coefficients:

$$\bar{h}_i = \frac{1}{12} \sum_{1-t,b}^{6-t,b} h_{i_{t,b}} \qquad (4)$$

### 3.2 Dimensionless Parameters of the System

To understand the relative importance of the various time scales and forces involved, the dimensionless parameters of the system are presented. The Nusselt number is calculated based upon the overall heat transfer coefficient and hydraulic diameter of the annular gap between the electrode and the inside of the stainless steel heat exchanger tube, $D_h = D_i - D_e$, such that,

$$Nu_{D_h} = \frac{\bar{h}_i D_h}{k_L} \tag{5}$$

where $D_e$ is the electrode diameter and $k_L$ is the saturated liquid refrigerant thermal conductivity. In a like manner, the Reynolds number is defined according to:

$$\mathrm{Re}_{D_h} = \frac{\dot{m} D_h}{A_i \mu_L} \tag{6}$$

where $\dot{m}$ is the refrigerant mass flow rate and $A_i$ is the tube-electrode annular cross section area.

The charge relaxation time, $\tau$, is a measure of the rate at which free charges relax from the bulk of the fluid to the outer boundaries of a dielectric mass. In the context of this AC investigation it is an important time scale because it gives a sense of the fluids free charge responsiveness when subject changes in the electric field environment, for a fluid of continuous properties it is defined as $\tau = \varepsilon/\sigma_{e-}$. For an AC voltage at a prescribed frequency, $f$, the comparison of the inverse of the electric field frequency (twice the applied voltage frequency) against the charge relaxation time leads to the ratio of time scales given as,

$$T_r = \frac{\tau}{1/f} = \tau\, f \tag{7}$$

The time scale ratio provides an order of magnitude estimate of the relative importance of the first two force terms of electrical origin in Equation (1). That is, if the ratio is much larger than unity, f>>1/τ, free charge does not have sufficient time to build up in the fluid and therefore cannot be acted upon by the electric field. Thus the electrophoretic force may be negligible compared to the dielectrophoretic force within the liquid phase [3].

The electric body force may be represented by two dimensionless numbers [2,8];

$$E_{hd} = \frac{I_o L^3}{\rho_o \nu^2 \mu_c A} \qquad \textit{the EHD Number} \tag{8}$$

$$M_d = \frac{\varepsilon_o E_o^2 T_o (\partial \varepsilon_s / \partial T)_\rho L^2}{2 \rho_o \nu^2} \qquad \textit{the Masuda Number} \tag{9}$$

Scaling arguments show that the combined effects of electrically induced flow and forced convection must be considered when $E_{hd}/Re_L^2 \sim 1$ and/or $M_d/Re_L^2 \sim 1$, which are analogous to the Richardson number for mixed forced and natural convective flows. In Eqs. 8 and 9 the reference electric field is taken to be the electrode surface, the reference length is annular gap of the concentric electrodes and the gradient of the specific dielectric constant is approximated as the slope of the Gurova et al. [36] correlation.

### 3.3 Uncertainty Analysis

Table 2 lists the measurement uncertainty associated with the various measurement devices. For accurate determination of the heat transfer coefficient quite accurate temperature measurements are required. To avoid unwanted interference between the high voltage system and the thermocouple measurement system, as well as additional cold junction compensation errors, a specialized ice bath was constructed to the specifications outlined in ASTMSTP 470 (1970). The bath is known to be isothermal and maintain a constant temperature of 0.01 °C, as the standard specifies. The total *emf* was then converted to a temperature measurement using individual system calibration curves for each thermocouple. The calibrated accuracy was within ±0.1°C as shown in Table 3.

For the purpose of uncertainty calculation, each measurement is denoted by $x_i$ and the uncertainty in the measurement $w_i$. The result of a calculation using these measurements is denoted Z and the uncertainty in the calculated result is denoted by $w_z$. The uncertainty $w_z$ is calculated using the method of Kline and McClintock [37] using the following equation:

$$w_z = \sqrt{\left(\sum_{i=1}^{n}\left[\frac{\partial Z}{\partial x_i} w_i\right]^2\right)} \qquad (10)$$

The maximum experimental uncertainties are summarized in Table 3.

## 4.0 Results and Discussion

### 4.1 The Overall Influence of an AC Applied Voltage

The primary aim of this study is to gain a better understanding of the interaction between EHD forces and a two phase flow. In particular, how the EHD forces alter the flow regime and cause changes in the heat transfer characteristics of the heat exchanger. To do so, the interactions are examined by considering the effect of the flow regime on both the quasi-local and overall averaged heat transfer characteristics of the heat exchanger, as well as the overall pressure drop.

Resolving the equations of electrohydrodynamics through dimensional analysis was used to elucidate flow behaviour that could not be directly derived or simulated. Quantifying the importance of each component has not been possible because of the complicated nature of convective boiling. The dimensionless analysis performed in a previous study included such an analysis for DC applied voltages [8] which provide an indication of the condition where significant EHD influences on the base flow may be expected. An order of magnitude comparison of the electric field induced forces and the inertial forces suggest that EHD influences on the flow of liquid in the channel may be expected for the case when $E_{hd}/Re_L^2 \geq 0.1$ and/or $M_d/Re_L^2 \geq 0.1$ due to an electric field. The ratios suggest that the EHD forces will dominate over inertial ones for low flow rates, well into the laminar regime, with an applied voltage greater than about 6.0 kV. In addition, it also suggests that for $Re_L > 20,000$ or $V_i \geq 2$ kV the nature of the flow will be determined primarily by inertial forces within the fluid and EHD forces will not be strong enough to alter the flow. Further, the study suggested that for the DC conditions considered, $E_{hd}$, thus the electrophoretic force, is unlikely to play a significant role in augmenting the flow.

This work studies both low frequency (60 Hz) and high frequency (6.6 kHz) AC voltages (i) in order to investigate the dimensional analysis prediction that the dominant force was dielectrophoretic in nature and (ii) to explore an underdeveloped field of AC electrohydrodynamics in two-phase heat transfer applications.

For this AC study, applying the concept of electrical charge relaxation time, $\tau=\varepsilon/\sigma_e$, provides insight into the mechanisms of electrically induced motion in the liquid-phase [3,7,38] and is used to indicate whether the dielectrophoretic force dominates the electrically induced flow. Unfortunately, limited electrical characterization data is available and it is thus difficult to establish the charge relaxation time over a large range of frequencies. Considering the time ratio at 1000Hz (the only frequency data available Table 1), the relaxation time is estimated to be $\tau$~0.2ms and a time scales ratio of approximately $T_r \sim 0.4$. As electrical resistance decreases significantly with frequency for R134a, as the frequency is increased to 6.6kHz, the range tested in the current investigation, a reduction $T_r$ and thus the intensity of the electrophoretic force component is expected. Thus for electrically induced motion to exist, other body forces must be dominant.

Fig. 4 shows a comparison of the experimental heat transfer and pressure drop data for both the DC and AC tests. The Masuda numbers for the AC tests are based on the voltage amplitude, not the RMS voltage, because the oscillating voltage results in unique dynamic two-phase flow patterns.

Fig. 4 shows that for the 60 Hz AC case the heat transfer and pressure drop levels are notably lower compared to the DC and high frequency AC conditions. Consistent with the observations discussed in Cotton et al. [39] high speed photography at the exit revealed an oscillatory flow, where droplets as large as 2 mm in diameter were entrained in a vapour core surrounded by annular liquid films covering both the tube and electrode surfaces; similar to a multi-layered annular flow. The suspended droplets moved axially along the lower portion of the annulus with the main flow whilst oscillating vertically at a frequency of approximately 120 Hz. The droplets were occasionally absorbed by the inner or outer annular films. In addition to the droplet formation, small conical spouts, resembling jets of liquid, appeared on the upper half of the annular film of the electrode. The spouts were observed to form randomly on wave crests created by interfacial instabilities and would spray a fine mist into the upper portion of the vapour core. It is possible that these structures are similar in nature to the classic Taylor cone with the mist being the resulting atomized electrospray [40].

The size of the droplets, intensity of motion, rate of deposition and the occurrence of spouts were highly dependent on the amplitude of the 60 Hz applied voltage and the Reynolds number. For high voltage amplitudes, the suspended droplets tended to be much smaller creating a significant level of mixing at the heat transfer surface. The interaction between the phases, the extremely high interfacial area created and the increased mixing caused by the oscillatory motion of the flow led to significant increases in the Nusselt number (~3 fold) for the lowest flow rate ($Re_L$=3500) with a similar increase in the overall pressure drop, as seen in Fig. 4. As will be discussed, the heat transfer enhancement is not as pronounced for the higher Reynolds number case due to the increased relative influence of inertial forces over the EHD forces.

For the DC tests [8, 9], the heat transfer coefficient and pressure drop both increase with increasing voltage levels and the trend is well approximated by $Nu \propto M_d$ and $\Delta P \propto M_d$, respectively. The 6.6kHz tests show a similar trend and are in quantitative agreement with the DC results suggesting that this high frequency AC scenario is electrically equivalent to DC, albeit the range of $M_d$ is limited for the high frequency AC tests. For the 60 Hz tests, the dependence of $Nu$ on $M_d$ is not linear and the exponent for the functional relationship $Nu \propto M_d^n$ depends on $Re$, with n>1 for Re=3500 and n<1 for Re=11200.

The 60 Hz heat transfer results are consistently lower than the DC results, when compared using the voltage amplitude of the AC waveforms in the calculation of the Masuda number. This would suggest that the flow regime consisting of the suspended oscillating droplets is not as effective with regard to improving the heat transfer. This is likely due to the short duration of the applied voltage being less able to extract liquid from the stratified layer thus resulting in a thicker stratified layer at the bottom of the tube.

The frequency of the vertical droplet fluctuations, determined through high speed video imaging, was approximately 120 Hz. This corresponds to twice the frequency of the applied voltage frequency of $f$ ~ 60 Hz. This is roughly the frequency of the "on" and "off" dielectrophoretic body force that is developed at this voltage frequency, as $f_E \propto E^2$. This pattern suggests that the fluctuations in the flow pattern are actually the continuous transition between flow regimes due to the oscillation of the electric field. It is postulated that the resultant flow regime is the continuous construction and destruction of two separate flow regimes. For example, at $Re_L=3500$ the flow pattern in the absence of the electric field is dominantly stratified flow which changes to intermittent annular with entrained droplets as the DC voltage level is increased. In addition, for high voltage amplitudes (>10kV) additional instabilities lead to droplet break up and significant agitation of the annular film resulting in an increase in the rate at which both the heat transfer and pressure drop increase.

Fig. 4 also compares the effect of increasing the applied voltage level at different Reynolds numbers. Similar to the DC experiments detailed in [8], under the influence of a 60 Hz AC electric field, the EHD forces must overcome inertial, surface tension and gravity forces in order to produce a migration of the liquid. As the Reynolds number increases, the relative influence of the inertial forces will increase disproportionately considering the scale of the ratio $M_d/Re_L^2$. As a result, the 60 Hz AC EHD forces did not dominate the flow at $Re_L=11200$ and the oscillatory motion observed at $Re_L=3500$ was not observed at the exit of the channel. The result is an asymptotic trend in the heat transfer with a relatively low level of enhancement. The pressure drop across the channel increases linearly and at a lower rate compared with the DC tests.

In summary, for the range of parameters tested the 60 Hz AC tests resulted in a 3-fold increases in the Nusselt number and overall pressure drop for $Re_L=3500$. Furthermore, for the lower Reynolds number tests the use of 60Hz AC resulted in a 25% higher Nusselt number compared to the maximum DC voltage case. For the $Re_L=11200$ tests, Fig. 4a shows that for the 60Hz AC tests the Nusselt number results initially increase with $M_d$ up to an enhancement in the region of 1.5-fold where it tends to plateau. Conversely, the Nusselt number increases nearly linearly with increased DC voltage to a maximum of 2-fold, though tests were not performed beyond this point as the breakdown voltage of the working fluid was being approached. Interestingly, for this higher Reynolds number the pressure drop curves follow nearly the same profile indicating that, compared with the AC tests, DC produces better enhancement for the same or smaller pressure drop penalty.

### 4.2 The Local Influence of an AC Applied Voltage

Both local and transient analyses are presented in this section for the following conditions: $Re_L=3500$, $x_{in}=0\%$, and $q''=10.2\ kW/m^2$ for different AC voltage amplitudes. Fig. 5 shows the heat transfer coefficient distribution along the top and bottom sections of the tube for the DC and 6.6 kHz AC tests, whilst Fig. 6 shows the same data but for the 60 Hz AC tests.

Considering the 6.6 kHz AC experimental results shown in Fig. 5, the similarity between DC and high frequency applied voltages is evident. Comparing these to the results of the 60 Hz AC quasi-local data in Fig. 6, considerably improved heat transfer enhancement is apparent, especially at the 12.4 kV voltage amplitude case. Compared with the field-free case, the overall enhancement with 12.4 kV applied voltage is approximately 3-fold, with local heat transfer enhancements exceeding 4-fold near the outlet of the channel.

For these test conditions, dynamic measurements and flow mapping suggest that the dominant flow pattern for the field-free case is stratified wavy. One would thus expect a significant difference in heat transfer coefficients between the top to the bottom of the tube. This is in fact what is observed in Fig 5. For the DC and 6.6 kHz AC the local heat transfer coefficients increase with increased applied voltage for both the top and bottom sections, except at the tube entrance. For the 60 Hz AC tests and $V \leq 9.2$ kV, Fig. 5 shows a similar trend for the bottom section. The heat transfer coefficients at the top of the tube, however, are not notably influenced by increasing the applied voltage until V ≤ 9.2 kV where there is an increase at the end portion of the tube. Again, by considering the interfacial forces as EHD is applied to the flow, the dielectrophoretic force can create instabilities on the interface resulting in a significantly more disturbed flow with larger more frequent waves, which are expected to be amplified by the fluctuating AC electric field. If the EHD effect becomes significant, then migration of the liquid may occur. Therefore, when the liquid is attracted away from the stratified liquid layer towards the electrode against gravity, the result is a reduction in the liquid thickness and thermal resistance on the bottom of the tube which is considered to be the mechanism of enhancement for the bottom heat transfer coefficients. However, the liquid extracted from the bottom layer is observed to be suspended in the vapour core, thus not wetting the top surface, which may account for the lack of enhancement for the top section.

For the 12.4 kV case the heat transfer coefficient distribution changes considerably. For the bottom section there is a great deal of enhancement at the tube entrance which was not observed for the lower voltage levels. The top section shows a similar distribution in the heat transfer coefficient so that overall, the local heat transfer around the tube is much more symmetric and considerably enhanced compared with the field-free case. The predominant flow regime is now believed to be a destabilized oscillatory-entrained droplet flow discussed above. This flow pattern is more complex and transitional than traditional two-phase flow regimes, involving considerable phase interaction and interfacial area due to the vertical flow oscillations, large droplet entrainment and a liquid film encompassing the electrode. The end result being significant heat transfer enhancement and more uniform heat transfer around the tube circumference. To gain deeper insight into the apparent flow regime transitions, the transient local temperature measurements are examined in more detail in the following section.

**4.3 Wall Surface Temperature Profiles in the Presence of a 60 Hz Applied Voltage**

Fig. 7a shows the time averaged axial wall superheat profiles for the same flow conditions as the DC cases considered in [8] for three 60 Hz AC voltage amplitudes (6.2 kV, 9.2 kV and 12.4 kV) and the 0 kV case. Fig. 7b shows the corresponding standard deviations of the superheat fluctuations. A higher standard deviation indicates that the temperature at that point fluctuated more about the corresponding time-averaged value over the course of the sampling period. Standard deviations in the range of ± 0.05 ~ 0.08°C may be assumed to represent a constant temperature reading since this variation in temperature is in the order typical of white noise fluctuation.

The wall superheat plots at locations 1 through 6 in Fig. 7a show that the application of a 60 Hz AC voltage decreases the wall superheat on both the top and bottom of the channel, though the effect is more pronounced for the top surface region. Fig. 7b shows that wall superheat fluctuations for the bottom of the tube are low enough to be considered constant, and this does not change with the application of an applied voltage. This suggests a continually wetted bottom surface along the entire channel which is confirmed with the visual observations from the high speed videos at the outlet. The top surface shows notably higher temperature fluctuations, indicating intermittent wetting, as well as a stronger sensitivity to the applied voltage level. For the 0 kV case the top wall superheat fluctuations are negligibly small between the entrance and mid region (location 1 and 2) and then increases with axial distance from the centre to the tube exit region. With increased voltage potential the fluctuations in the mid to exit region become progressively less, indicating that there is improved wetting of the top surface, to the extent that for 12.4 kV there are no apparent fluctuations and the top surface can be considered wetted over this region. In fact, for the 12.4 kV case the entire top and bottom sections of the tube are continually wetted. Interestingly, the intermediate voltage potentials ($V_i$*=6.2 kV* and $V_i$*=9.2 kV*) show an increase in the superheat fluctuations on the upper surface with increasing voltage at the entrance (location 1).

Similar to observed DC influences that tend to increase the upper temperature variation at location 1, the migration, deformation and breaking of vapour bubbles in the flow are the main contributing factors augmenting bubble dynamics and as a consequence the wall temperature variation in this region. By combining the dynamic effects of the 60 Hz electric field strength variation with the various EHD effects on nucleate boiling, these influences are expected to be accentuated, thereby increasing the temperature variations accordingly. This is corroborated by the recent work of Liu et al [39] and Siedel et al [40] who have shown, respectively, that EHD can significantly augment the heat transfer and bubble dynamics during nucleate pool boiling.

Downstream of the entrance where there is significant void in the channel (i.e. locations 2 to 6), the electric field creates a force at the vapour-liquid interface enhancing the momentum suction pressure effect, thereby attracting the liquid upwards towards the electrode. The liquid layer at the bottom thus becomes thinner which decreases the thermal resistance at the bottom surface, causing the temperature of the wall to drop and the heat flux to increase. This effect is apparent from the measured increase of the heat transfer coefficients and the lower wall superheats along the lower half of the tube, as shown in Figs. 6b and 7a, respectively. As discussed, increasing the 60 Hz voltage amplitude causes both the upper wall superheats and the fluctuations to decrease, to the point of the fluctuations being negligible for the highest voltage tested. This is contrary to the effect of the DC voltage potentials, where the flow changes to large amplitude wave flow or slug flow with significant superheat fluctuations. For the current scenario, the flow is more likely a considerably agitated stratified wavy flow, where the liquid is attracted as high as the electrode when the electric field is "on" and drops back when the field is "off" during a period associated with the electric field strength squared (i.e. $E^2$ frequency ~120 Hz as shown in Fig. 4). The decrease in the top temperature is postulated to be either from an increased vapour circulation slightly increasing the heat transfer coefficient, Fig. 6, or more likely from the entrainment of small liquid droplets from the agitated waves creating a fine mist that continuously impinges the upper surface.

As mentioned, the top and bottom wall temperature measurements are almost identical at the tube exit region (location 6) for the 9.2 kV case. This is the case for the entire tube length for the 12.4 kV applied voltage tests. Consequently, the quasi-local heat transfer values are relatively uniform around the circumference of the tube at these locations. This implies a circumferentially uniform flow regime has developed because of the fluctuating electric field.

### 4.4 Flow Pattern Reconstruction

The flow pattern reconstruction for the DC electric field tests is detailed by Cotton et al [8] and will only be summarized here. For the 0 kV base case and 0% inlet quality (same as top schematic in Fig. 8) the dominant flow pattern is stratified wavy flow with large amplitude waves forming closer to the exit. This creates a stratified wavy/slug flow regime with large amplitude waves in this region. With intermediate applied DC voltage the onset of this flow regime moves closer to the inlet with significant droplet entrainment in the vapour core. Increasing the DC voltage further causes a higher concentration of entrained droplets in the vapour core. This reduces the liquid volume and thickness on the bottom layer returning it to a stratified wavy regime. The increased evaporation coupled with the more rigorous liquid extraction tends to almost completely consume the bottom liquid layer by the test section exit and a dispersed droplet/annular flow exists in this region.

For the intermediate AC voltage amplitudes of 6.2 kV and 9.2 kV the wall superheats were observed to decrease moderately from the field-free case. Therefore, it is presumed that a major flow regime transition had not yet occurred. The moderate superheat reductions and differences in their standard deviation are likely due to increased amounts of entrained droplets. The only significant difference is at the exit region (location 6) for the 9.2 kV test, where the top wall temperature decreased significantly to approximately that of the diametrically opposed bottom wall superheat. This being the case, the flow pattern is believed to be circumferentially uniform around the tube and, with the support of high speed video imaging at the exit viewing window, this regime was identified as an oscillatory-entrained droplet flow pattern.

Increasing the voltage amplitude to 12.4 kV results in a significant change in the behaviour of the wall superheats, as shown in Fig. 7. Here, the wall superheats drop to a point where they are almost uniform, both axially and circumferentially. The upper half of the channel decreased by approximately 5 °C and the lower half of the channel by about 2 °C below the field-free case. Further, the superheat fluctuations are all within the band of white noise which signifies that the tube wall is continuously wetted. Similar to the 9.2 kV case, the exit flow regime observed visually was an oscillatory-entrained droplet flow pattern. Based on the homogeneity of the surface temperatures, the oscillatory-entrained droplet flow has likely developed throughout the entire heat exchanger, with the exception of possibly location 1, where the quality is quite low at x ~ 4%. At the entrance region, the flow is similar to that observed for the highest DC voltage cases, dispersed bubbly flow, as discussed in [8].

The complex nature of the oscillatory flow pattern results in an augmentation in both phase interaction and interfacial area due to the vertical flow oscillations, the high level of droplet entrainment and the liquid film encompassing the electrode. A uniform rate of heat transfer is evident in Fig. 6 because of the apparent symmetry in the prevailing flow pattern, confirmed with the high speed video footage. The schematics of the proposed flow pattern reconstruction both in the absence of an electric field and at increasing 60 Hz AC applied voltages are presented in Fig. 8.

**5. Conclusion**

Agreement between the DC and 6.6 kHz AC results at a duty cycle of approximately 90% suggests that the electrophoretic component of the electric body force may not be significant. Therefore, for electrically induced motion to exist, other body forces must be dominant and has been deduced to be the dielectrophoretic force for the DC and high frequency AC cases.

The EHD forces created by the application of the 60 Hz AC voltage created an oscillatory flow regime as observed in the outlet section of the test section. Based on visual observation, the oscillations of the flow pattern are suspected to be the continuous transition between flow regimes due to the approximate "on/off" electric field applied to the electrode. The resultant flow regime is quite unique and is postulated to be due to the continuous construction and destruction of two limiting flow regimes. The interaction between the phases and the resulting interfacial area was extremely high, which, when coupled with the increased mixing created by the oscillatory motion of the flow, in some cases led to significant local enhancements in heat transfer. For these moderate frequencies, it is yet difficult to identify the dominant electric forces, partially due to the limited electrical properties available.

**Acknowledgments**

This work is partially supported by Dana Corporation, Long Manufacturing (JSC, MS, AJR), The Natural Science and Engineering Research Council of Canada (JC) and ASHRAE (JC, MS).

## References

[1] W. Panofsky, M. Phillips, Classical Electricity and Magnetism, 2nd ed., Addison-Wesley, Pub. Co., Reading, Massachusetts, 1962.

[2] J.S. Chang, A. Watson, Electromagnetic hydrodynamics, IEEE Trans. Dielectric. and Elec. Insu. 1 (5) (1994) 871 895.

[3] T.B. Jones, Electrohydrodynamically enhanced heat transfer in liquids - A review, Advances in Heat Transfer 14 (1978) 107-148.

[4] J.M.H. Peters, J.L. Sproston, G. Walker, Preliminary observations on bulk electroconvection in electrically stressed liquid insulants, Part I: Experimental investigation, J. of Electrostatics 8 (1980) 139-152.

[5] J.M.H. Peters, J.L. Sproston, G. Walker, Preliminary observations on bulk electroconvection in electrically stressed liquid insulants, Part II : Theoretical Investigation, J. of Electrostatics 9 (1980) 1-14.

[6] T. Fujino, Y. Yokoyama, Y.H. Mori, Augmentation of laminar forced convective heat transfer by the application of a transverse electric field, ASME J. Heat Transfer, 111 (1989) 345-351.

[7] A. Yabe, Heat engineering, Chapter 25, Handbook of Electrostatic Processes, J.S. Chang, A.J. Kelly, and J.M. Crowley, ed., Marcal Dekker, Inc., New York, (1995) 555-580.

[8] J.S. Cotton, A.J. Robinson, M. Shoukri, J.S. Chang, A two-phase flow pattern map for annular channels with and without a DC applied voltage and the application to electrohydrodynamic convective boiling analysis, Int. J. of Heat and Mass Transfer, 48 (25-26) (2005) 5536-5579.

[9] J.S. Cotton, A.J. Robinson, J.S. Chang, M. Shoukri, Electrohydrodynamic enhancement of flow boiling in an eccentric horizontal cylindrical channel, J. of Enhanced Heat Transfer 15 (3) (2008) 183-198.

[10] S. Laohalertdecha,S. Wongwises, Effects of EHD on heat transfer enhancement and pressure drop during two-phase condensation of pure R-134a at high mass flux in a horizontal micro-fin tube, Experimental Thermal and Fluid Science 30 (7) (2006) 675-686

[11] H. Sadek, J.S. Cotton, C.Y Ching, M. Shoukri, Effect of frequency on two-phase flow regimes under high-voltage AC electric fields, J. of Electrostatics 66 (1-2) (2007) 25-31.

[12] A. Singh, M.M. Ohadi, S. Dessiatoun, W. Chu, In-tube boiling heat transfer enhancement of R-123 using the EHD technique, ASHRAE Trans. 100 (2) (1994) 818–825.

[13] C. Norris, J.S. Cotton, M. Shoukri, J.S. Chang, T. Smith-Pollard, Electrohydrodynamic effects on flow redistribution and convective boiling in horizontal concentric tubes, ASHRAE Trans. 105 (1) (1999) 222–236.

[14] G.D. Harvel, B. Komeili, C.Y. Ching, J.S. Chang, Electrohydrodynamically Enhanced Capillary Evaporator, IEEE Transactions on Dielectrics and Electrical Insulation 16 (2) (2009) 456-462.

[15] P.H.G. Allen, T.G. Karayiannis, Review Paper: Electrohydrodynamic enhancement of heat transfer and fluid flow, Heat Recovery Systems and CHP, 15 (1995) 389-423.

[16] J. Seyed-Yagoobi, J.E. Bryan, Enhancement of heat transfer and mass transport in single-phase and two-phase flows with electrohydrodynamics, Advances in Heat Transfer, 33, (1999) 95-186.

[17] S. Laohalertdecha, P. Naphon, S. Wongwises, A review of electrohydrodynamic enhancement of heat transfer, Renewable and Sustainable Energy Reviews, 11*(5)*, (2007) 858-876.

[18] A. Yabe, T. Taketani, H. Maki, K. Takahashi, Y. Nakadai, Experimental study of electrohydrodynamically (EHD) enhanced evaporator for non-azeotropic mixtures, ASHRAE Trans, 98 (2) (1992) 455-461.

[19] A. Singh, M.M. Ohadi, S. Dessiatoun, M. Salehi, W. Chu, In-tube boiling enhancement of R-134a utilizing the electric field effect, 4th ASME/JSME Thermal Eng. Joint Conf., 2 (1995) 215-223.

[20] M. Salehi, M.M., Ohadi, S. Dessiatoun, The applicability of the EHD technique for convective boiling of refrigerant blends-experiments with R-404A, ASHRAE Trans., 102 (1) (1996) 839-844.

[21] J.E. Bryan, J. Seyed-Yagoobi, Influence of flow regime, heat flux, and mass flux on electrohydrodynamically enhanced convective boiling, J. Heat Transfer, 123 (2) (2001) 355-367.

[22] J. Berghmans, Prediction of the effect of electric fields on the most unstable wavelength during film boiling on small wires, J. Electrostatics, (1978) 5 265-272.

[23] T.B. Jones, K.R. Hallock, Surface wave model of EHD coupled minimum film boiling, J. Electrostatics, (1978) 5 273-284.

[24] A. Laures, R. Tobazéon, Electro-Optical Studies of Liquid Gaps Bridged by Insulating Spacers, IEEE Conference Publication No. 129, Dielectric Materials, Measurement and Application, (1975) 314.

[25] H. Sadek, A.J. Robinson, J.S Cotton, C.Y. Ching, M. Shoukri, Electrohydrodynamic enhancement of in-tube convective condensation heat transfer, Int. J. of Heat and Mass Transfer, 49 (9-10) (2006) 1647-1657.

[26] J.S. Cotton, Electrohydrodynamic Condensation Heat Transfer Modulation under dc and ac Applied Voltages in a Horizontal Annular Channel, IEEE Transactions on Dielectrics and Electrical Insulation, EHD Special Issue, (2009) 495-503.

[27] H. Sadek, J.S. Cotton, C.Y. Ching, M. Shoukri, , In-tube convective condensation under AC high voltage electric fields, 13th Int. Heat Transfer Conference (IHTC-13), Sydney, Australia, August, (2006) 190-199.

[28] I.W. McAllister, The dielectric strength of 1,1,1,2-C2 H2 F4 (Arcton-134a)," J. Phys. D: Appl. Phys., Letter to the Editor, 22 (1989) 1783-1784.

[29] B.R. Fellows, R.G. Richard, R.G., I.R. Shankland, Electrical characterization of alternative refrigerants," XVIIth Int. Cong. of Refrig., Montreal Convention Center, Montreal, Quebec, Canada, (45) (1991) 398-402.

[30] C. Meurer, G. Pietsch, M. Haacke, Electrical properties of CFC- and HCFC-substitutes, Int. J. of Refrigeration, 24 (2001) 171-175.

[31] T. Barao, U.V. Mardolcar, C.A. Nieto de Castro, The dielectric constant of liquid HFC 134a and HCFC 142b," Int. J. Thermophysics, 17 (3) (1996) 573-585.

[32] A. Sekiya, S. Misaki, The potential of hydrofluoroethers to replace CFCs and HCFCs and PFCs,  J. of Fluorine Chemistry, 101 (2001), 215-221.

[33] M. Spatz, B. Minor, HFO-1234yf low GWP refrigerant: A global sustainable solution for mobile air conditioning, SAE 2008 Alternative Refrigerant Systems Symposium, Presentation Material, June 10-12, Scottsdale, Arizona, US, (2008).

[34] R.G. Richard, Private Communication, June 14, 2000.

[35] Spatz, M. Minor, B., HFO-1234yf Low GWP Refrigerant: A Global Sustainable Solution for Mobile Air Conditioning, SAE 2008 Alternative Refrigerant Symposium, Presentation, June 10-12, 2008 Scottsdale, AZ (2008) 1-26.

[36] A.N Gurova, T. Barao, C.A Nieto de Castro, U.V. Mardolcar, The thermal conductivity and dielectric constant of HCFC-141b, HCFC-123, HCFC-142b, and HFC-134a," High Temp.-High Pres., 26 (1994) 25-34.

[37] S.J. Kline, F.A McClintock, Describing uncertainties in single sample experiments, Mech. Eng., (1953) 3-8.

[38] J.R. Melcher, Continuum Electromechanics, The MIT Press, Cambridge MA, USA (1981).

[39] J.S. Cotton, M. Shoukri, J.S. Chang, Oscillatory entrained droplet EHD two-phase flow, J. of Heat Transfer, 123 (8) (2001) 622.

[40] H. Park, K. Kim, S. Kim, Effects of a guard plate on the characteristics of an electrospray in the cone-jet mode, Journal of Aerosol Science 35 (2004) 1295–1312.

[41] Z. Liu, C. Herman, J. Kim, Heat transfer and bubble detachment in subcooled pool boiling from a downward-facing microheater array in a nonuniform electric field, Ann. N.Y. Acad. Sci. 1161 (2009) 182–191.

[42] S. Siedel, S. Cioulachtjian, A.J. Robinson, J. Bonjour, Electric field effects during nucleate boiling from an artificial nucleation site, Exp. Therm. Fluid Sci. (2010), doi:10.1016/j.expthermflusci.2010.06.006

**Nomenclature**

| | |
|---|---|
| A | surface area ($m^2$) |
| $C_p$ | specific heat (J/kg·K) |
| dP | pressure drop (Pa) |
| D | diameter (m) |
| $D_h$ | hydraulic diameter (m) |
| E | electric field strength (V/m) |
| $E_{hd}$ | EHD number (-) |
| f | frequency (Hz) |
| $f_E$ | electric force (N) |
| h | heat transfer coefficient ($W/m^2·K$) |
| I | current (A) |
| k | thermal conductivity (W/m·K) |
| L | length (m) |
| $\dot{m}$ | mass flow rate (kg/s) |
| $M_d$ | Masuda number (-) |
| Nu | Nusselt number (-) |
| P | pressure (Pa) |
| q | power (W) |
| $q^{//}$ | heat flux ($W/m^2$) |
| Re | Reynolds number (-) |
| T | temperature (K) |
| $T_r$ | time scale ratio (-) |
| $V_i$ | voltage applied to electrode (V) |

| | |
|---|---|
| $w_i$ | uncertainty in measurement |
| $w_z$ | uncertainty in calculated result |
| x | vapour quality |
| $x_i$ | measurement |
| Z | calculated variable |

Greek

| | |
|---|---|
| $\varepsilon$ | permittivity ($N/V^2$) |
| μ | viscosity (kg/m·s) |
| $\mu_c$ | ion mobility ($m^2/V \cdot s$) |
| $\rho$ | mass density ($kg/m^3$) |
| $\rho_{ei}$ | charge density ($C/m^3$) |
| τ | relaxation time (s) |
| $\nu$ | kinematic viscosity ($m^2/s$) |
| $\sigma_e$ | electrical conductivity (S/m) |

Subscripts

| | |
|---|---|
| a | average |
| b | bottom |
| e | electrode |
| E | electric |
| i | inner |
| in | inlet |
| L | liquid |
| o | reference |
| pp | peak to peak |
| S | surface |
| sat | saturation |
| t | top |

| | |
|---|---|
| T | temperature |
| V | vapour |
| W | water |

**TABLES and FIGURES**

**List of Captions**

**Tables**



**Figures:**

**Table 1:** Electrical Properties of R-134a

| | Electrical Property Data | Reference |
|---|---|---|
| Dielectric Breakdown (kV/mm) | 2.55<br>2.6<br>2.44 | McAllister [28]<br>Fellows et al. [29]<br>Meurer et al. [30] |
| Liquid Dielectric Constant @ ~20 ºC to 26 ºC | 9.51<br>9.46<br>9.0<br>9.2<br>9.8 | Fellows et al. [29]<br>Barao et al. [31]<br>Sekiya & Misaki [32]<br>Meurer et al. [30]<br>Spatz & Minor [33] |
| DC Resistivity (MΩ.m) | 7.3<br>9.6 | Sekiya & Misaki [32]<br>Spatz & Minor [33] |
| AC Resistivity (MΩ.m) @ 1 kHz | 1.77<br>2.5<br>1.09 | Fellows et al. [29]<br>Sekiya & Misaki [32]<br>Meurer et al. [30] |

**Table 2:** Measurement error

| **Parameter (Make, Type)** | **Error** |
|---|---|
| Temperature (calibrated)<br>(Type-T, Omega thermocouple) | ± 0.1 °C |
| Refrigerant Mass Flow Rate, high side<br>(FTB-101, Omega turbine flow meter) | 0.0313 ± 0.0002 kg/s (min)<br>0.1428 ± 0.0007 kg/s (max) |
| Refrigerant Mass Flow Rate, low side<br>(FTB-101, Omega turbine flow meter) | 0.00081 ± 0.00004 kg/s (min)<br>0.0183 ± 0.0001 kg/s (max) |
| Condensing Water Flow Rate<br>(F. & P. Rotameter) | 3.07± 0.06 kg/s (min)<br>10.2± 0.2 kg/s (min) |
| Heating Water Mass Flow Rate<br>(FTB-101, Omega turbine flow meter) | 0.03744 ± 0.0002 kg/s (min)<br>0.09871 ± 0.0005 kg/s (max) |
| Pressure Drop<br>(8.618 kPa, Validyne transducer) | 71.5 ± 0.1 Pa (min)<br>7639 ± 8 Pa (max) |
| Refrigerant Pressure<br>(Heise pressure sensor) | 620 ± 1 kPa (min)<br>680 ± 1 kPa (max) |
| Applied Voltage – DC (EHD)<br>(EL30R1.5, Glassman DC power supply) | 2.0 ± 0.2 kV (min)<br>8.0 ± 0.3 kV (max) |
| DC Current (EHD) | 0.5 ± 0.1 μA |

**Table 3:** Error of calculated result

| **Parameter** | **Maximum Percentage Error** |
|---|---|
| Heat Flux (W/m$^2$) | ± 10 % |
| Quality | ± 3 % |
| Heat Transfer Coefficient (W/m$^2$°C) | ± 14 % |

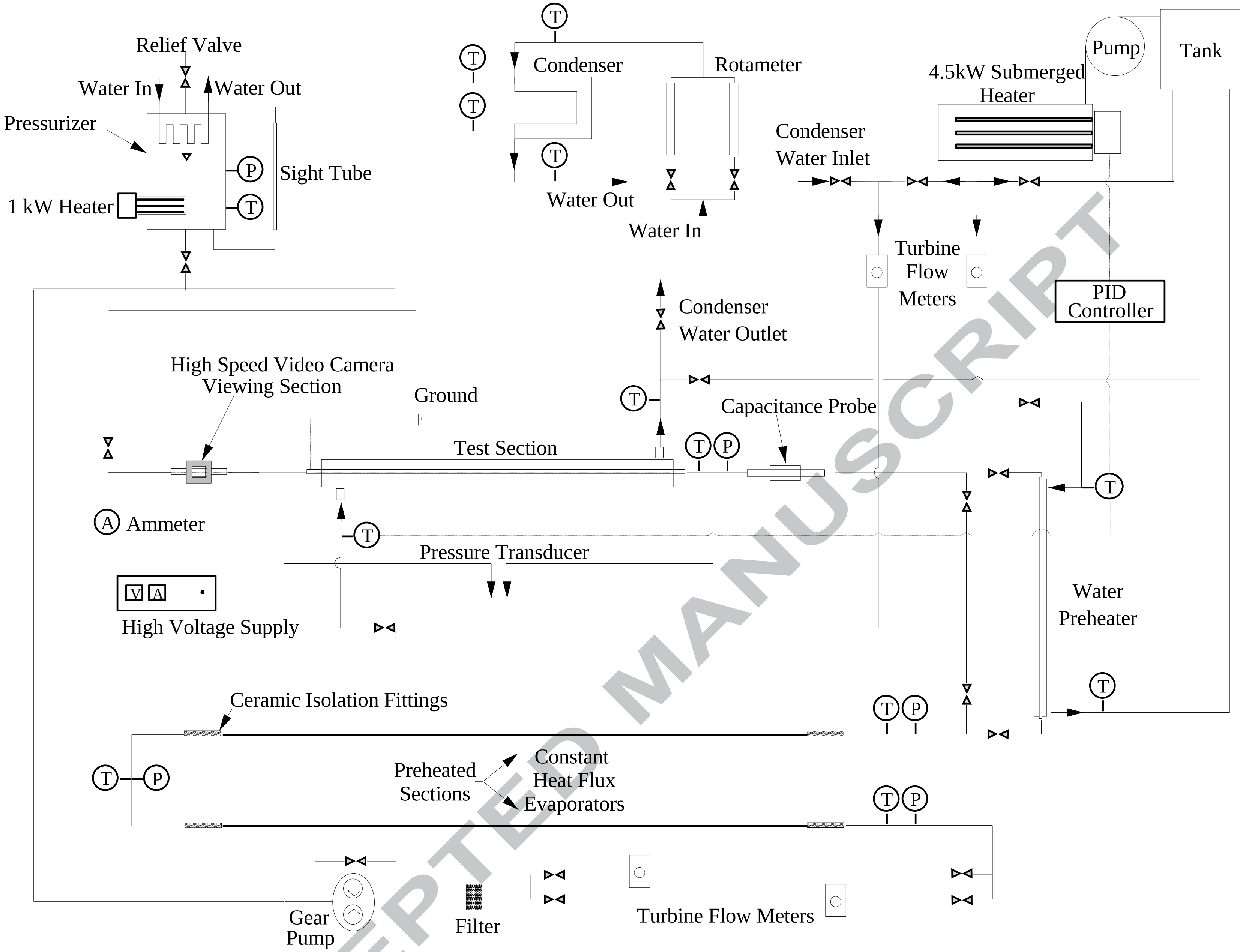


**Fig. 1:** Schematic Diagram of Test Facility.

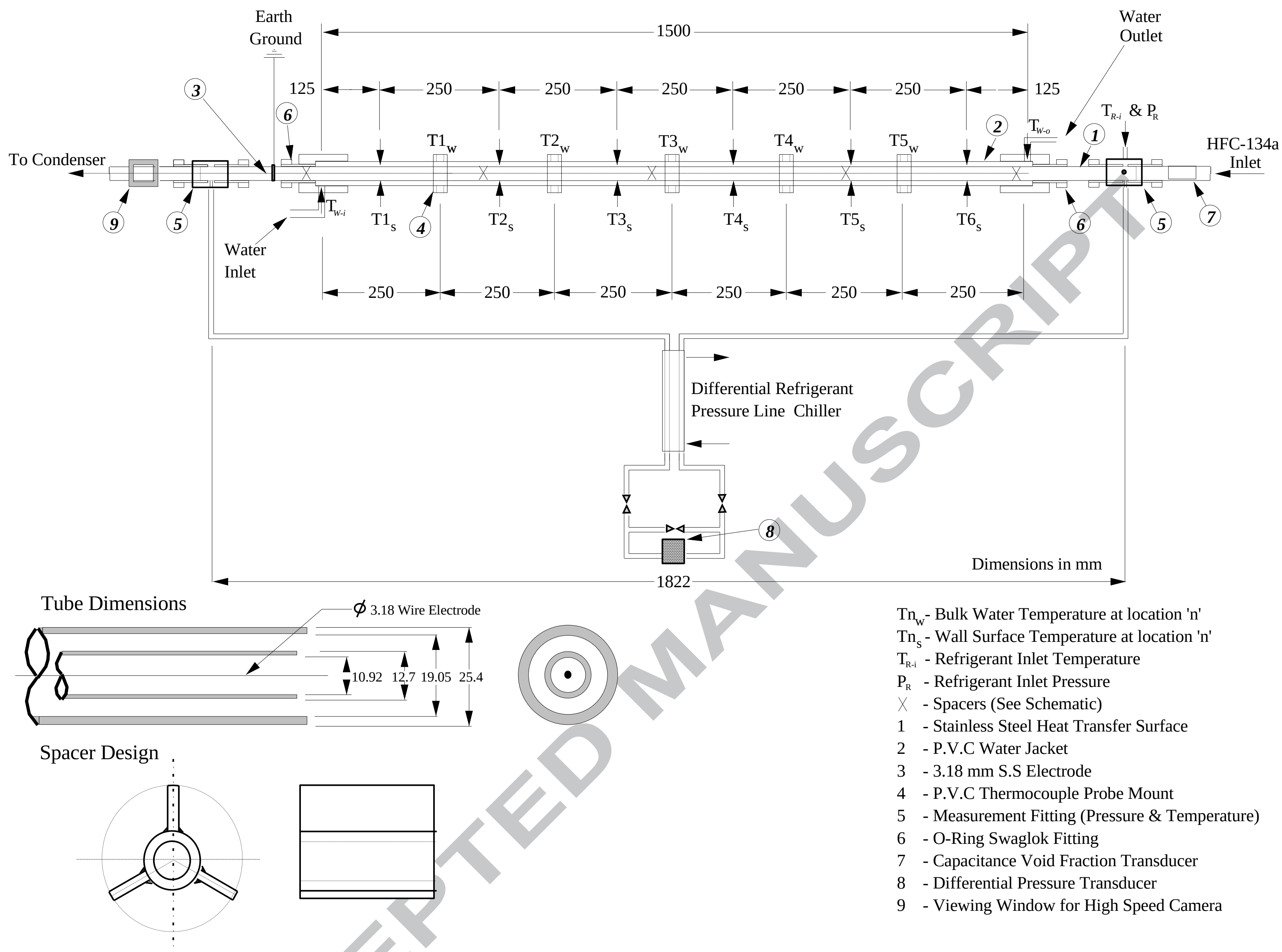


**Fig. 2:** Schematic Diagram of Test Section: The Electrohydrodynamic Heat Exchanger.

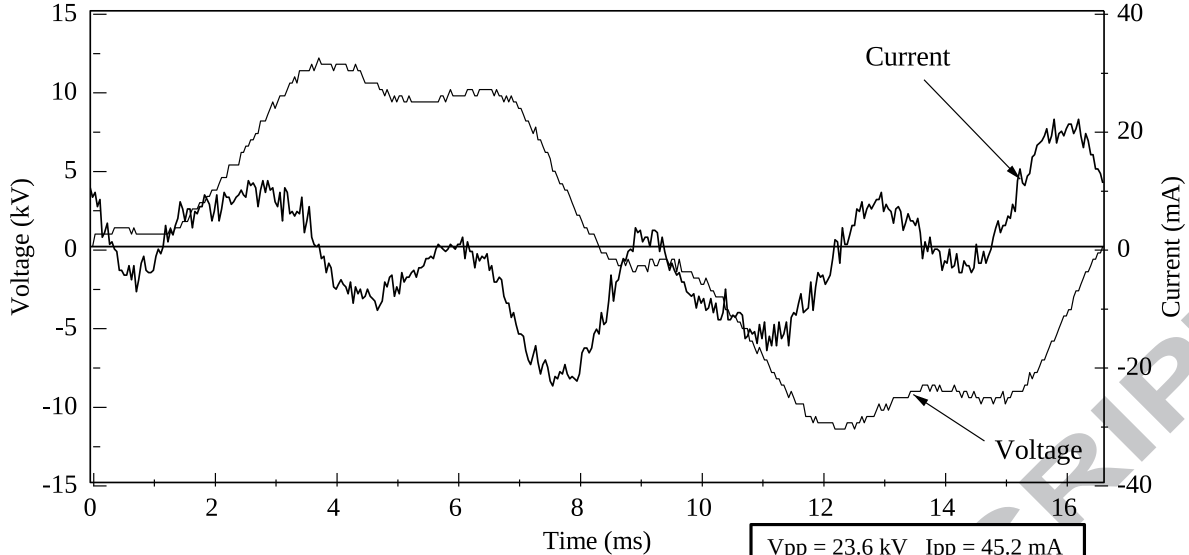


Vpp = 23.6 kV   Ipp = 45.2 mA
Va = 6.6 kV   Ief = 7.9 A

**a)**

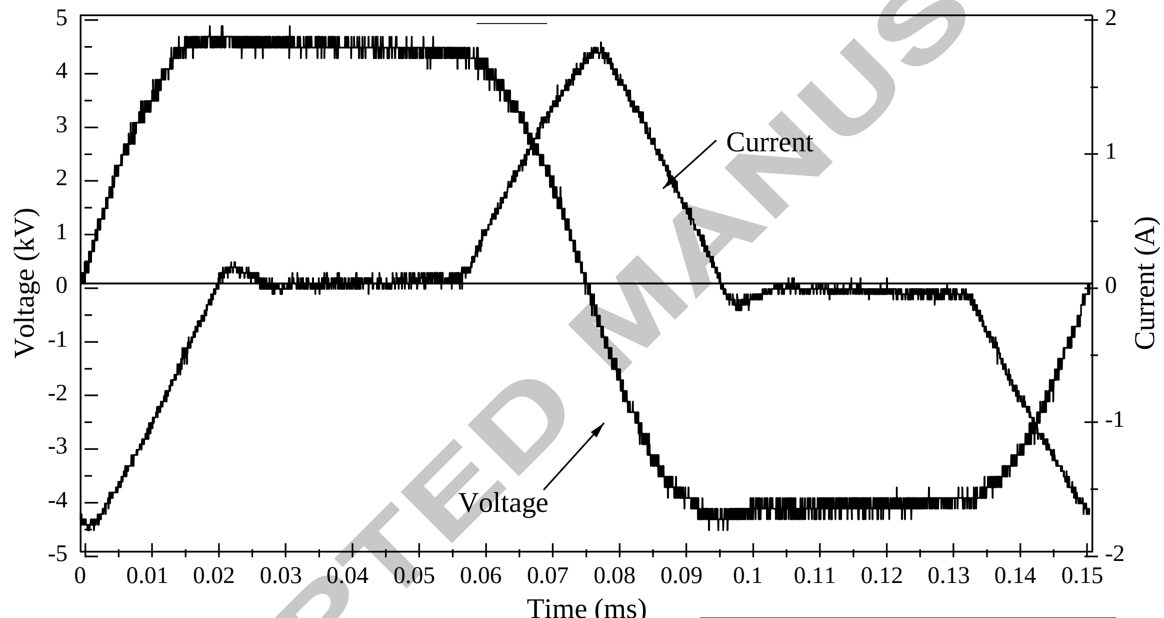


Vpp = 9.4 kV   Ipp = 3.6A
Va = 3.73 kV   Ia = 0.79A

**b)**

**Fig. 3**: Typical Current and Voltage Waveforms of the a) 60 Hz and b) the 6.6 kHz Transformer.

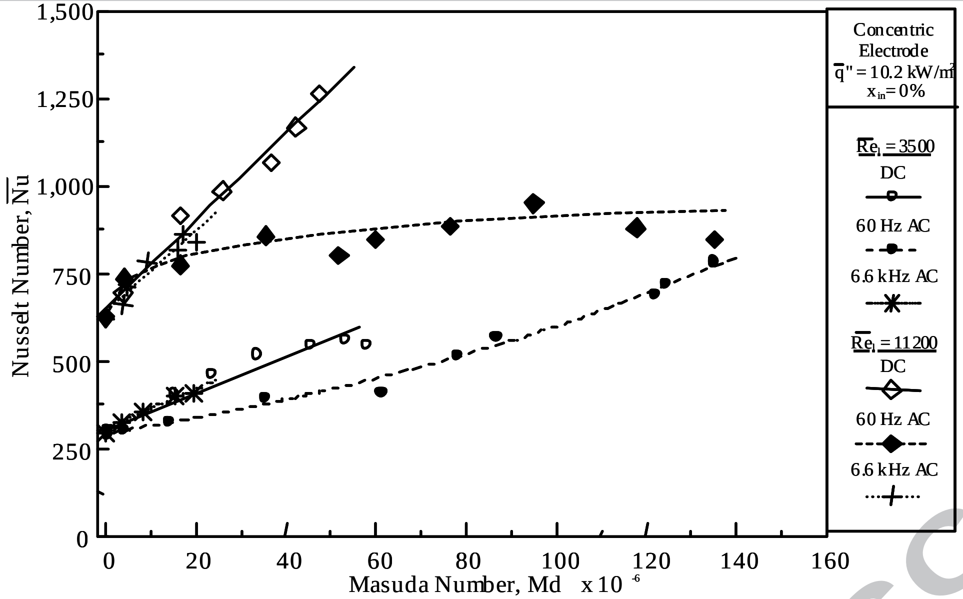


a) Nusselt Number vs. Masuda Number

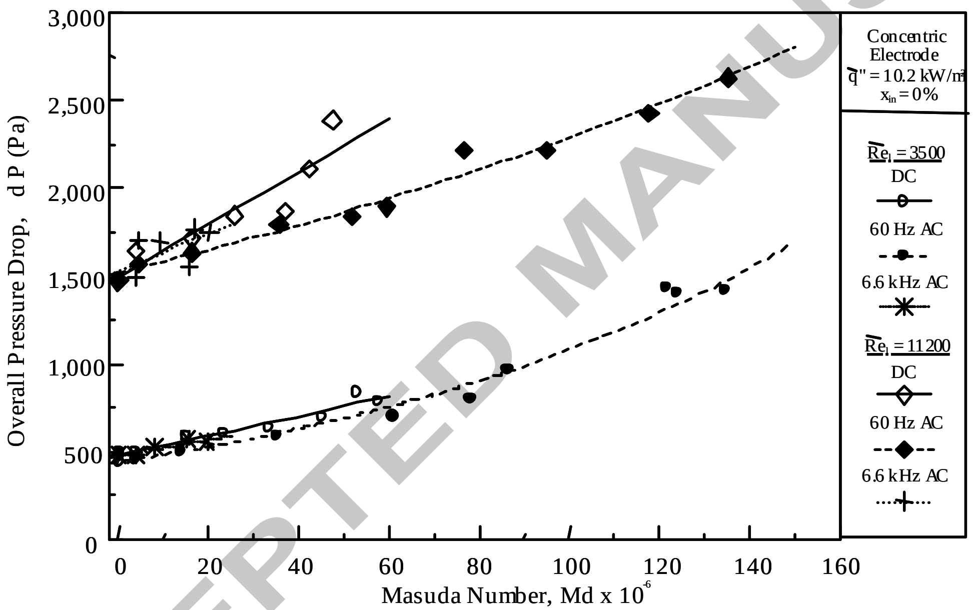


b) Overall Pressure Drop vs. Masuda Number

**Fig. 4**: The Effect of the DC & AC Masuda Numbers in liquid phase(based on the AC voltage amplitude) on the a) time-average a) Overall Nusselt Number and b) Overall Pressure Drop at a Fixed Heat Flux and Inlet Quality for two different Reynolds Numbers.

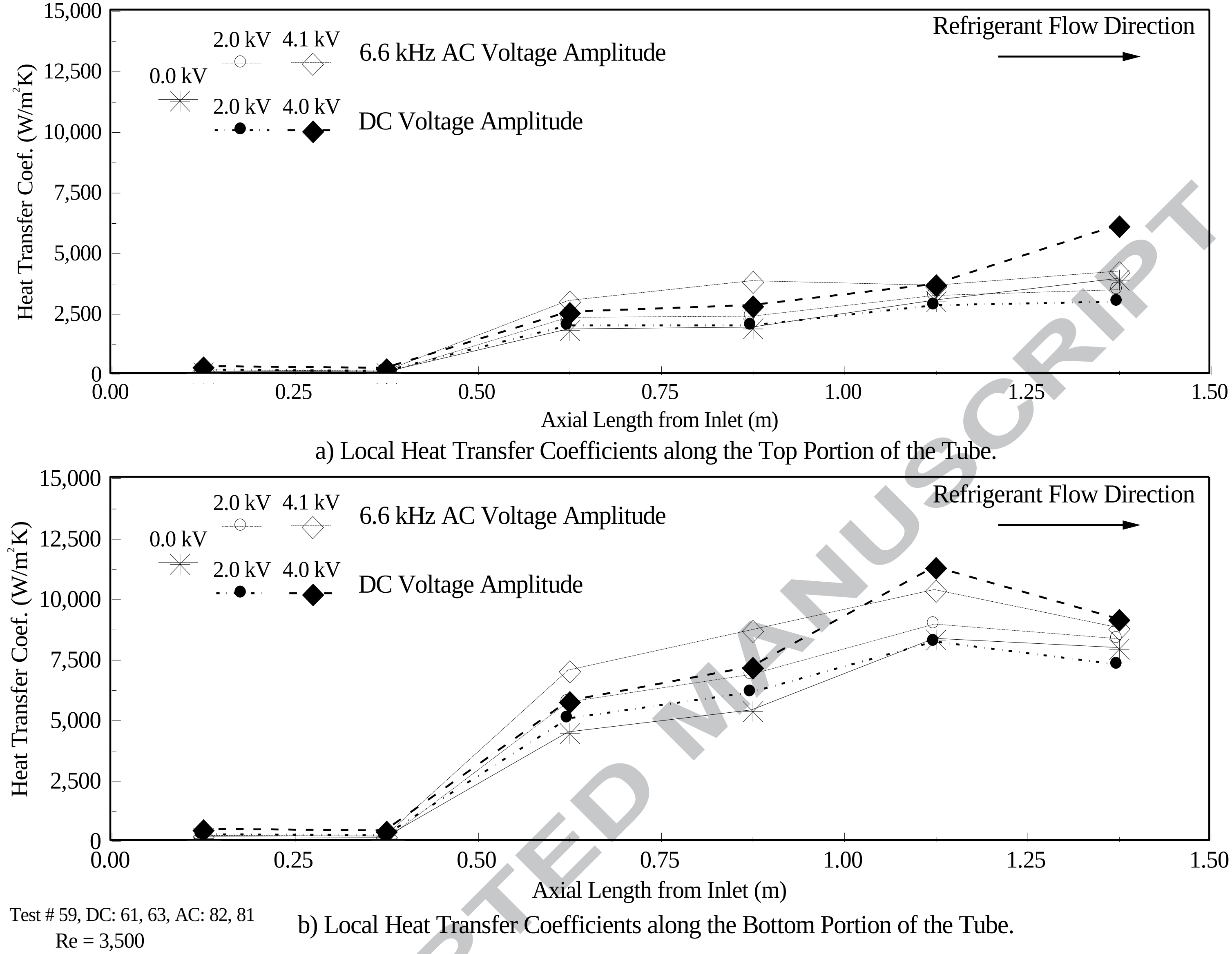


**Fig. 5:** A Comparison of the time and section averaged heat transfer coefficients along the axial direction for various DC and 6.6 kHz AC applied voltages (z=0 at inlet of heat exchanger).

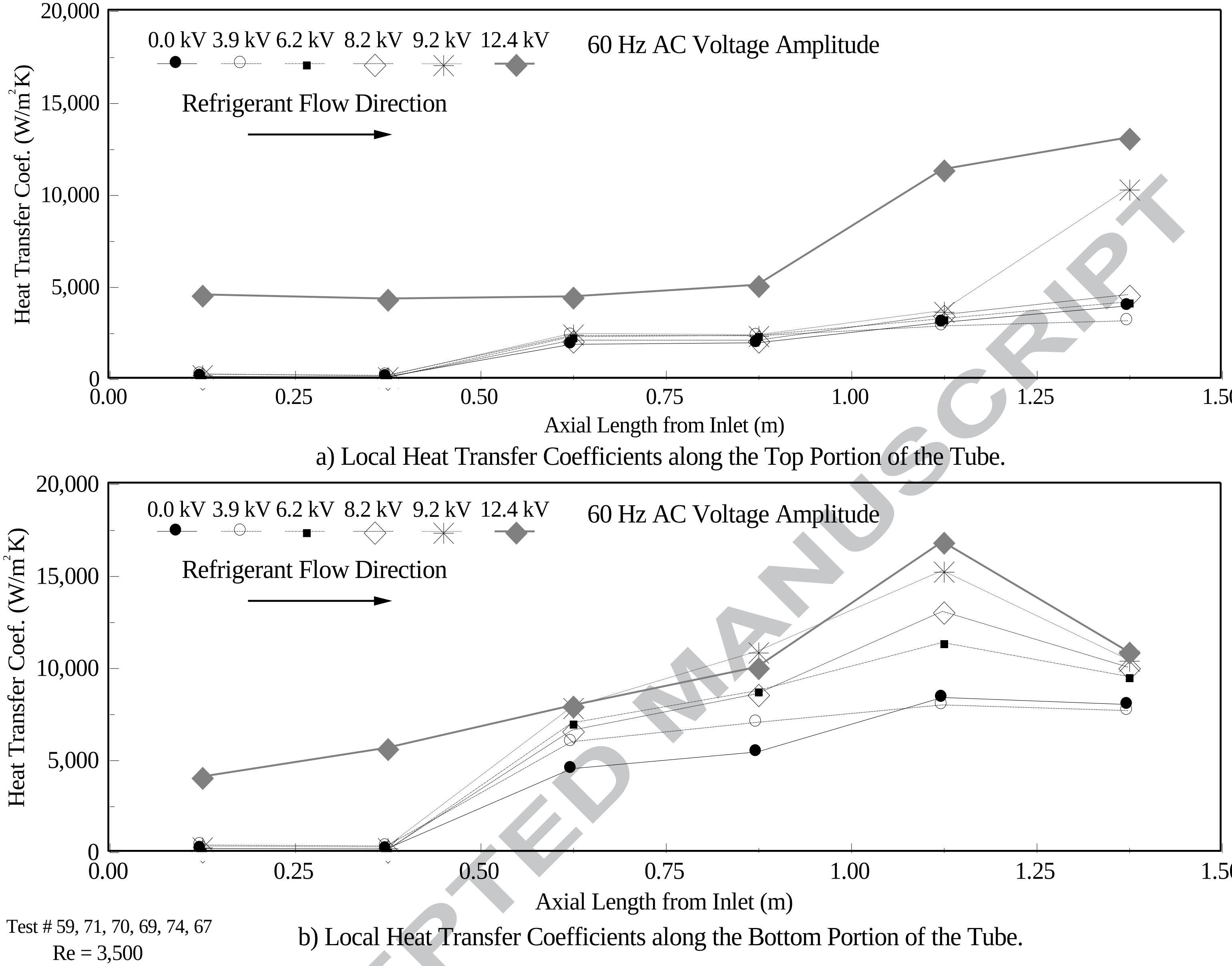


**Fig. 6**: A Comparison of the time and section averaged heat transfer coefficients along the axial direction for various 60 Hz AC applied voltages (z=0 at inlet of heat exchanger).

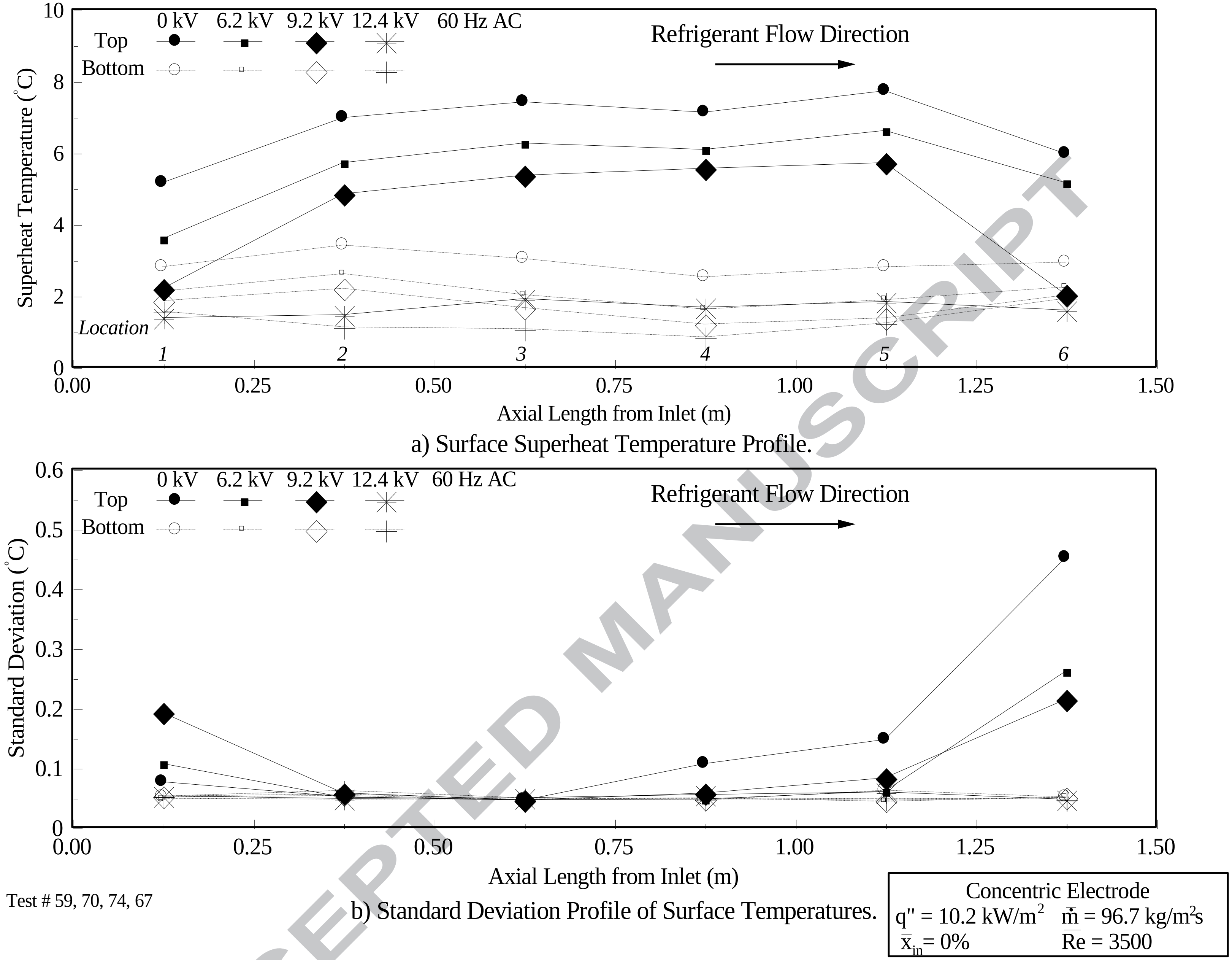


**Fig. 7:** Time-averaged axial surface superheat temperature and standard deviation profiles of the concentric electrode for various 60 Hz AC applied voltages.

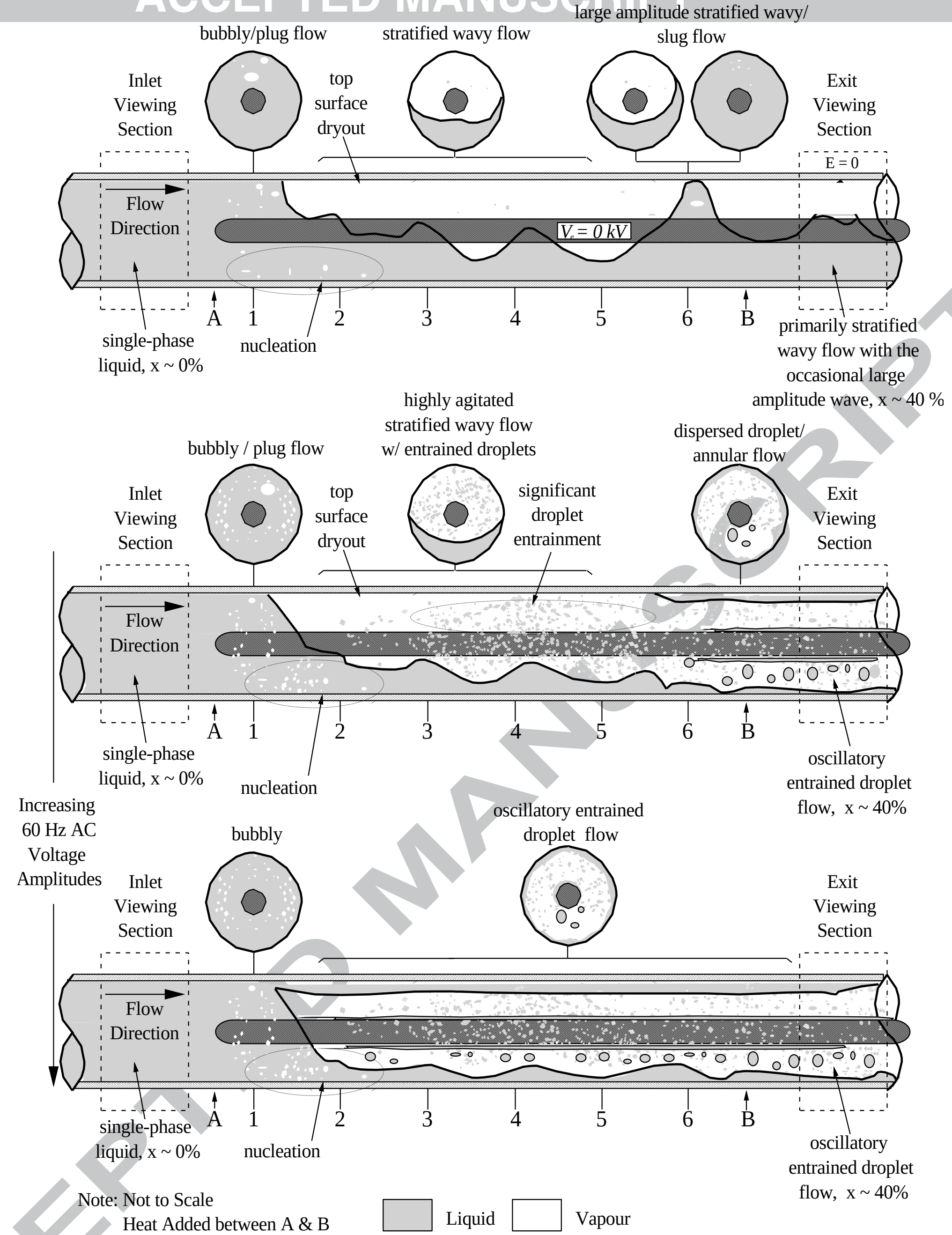


**Fig. 8:** Proposed Reconstructed Flow Pattern from Surface Temperature and Pressure Drop Traces and Inlet and Outlet Flow Regime Observations for Increasing 60 Hz AC Voltage Amplitudes ( $\dot{m}$ = 100 kg/m$^2$s, q" = 10.2 kW/m$^2$ and $x_{in}$ = 0%).